Available online at www.sciencedirect.com
ScienceDirect
Journal of Sound and Vibration 311 (2008) 1196–1212
JOURNAL OF SOUND AND VIBRATION
www.elsevier.com/locate/jsvi

The dynamics of three-dimensional underwater explosion bubble

A.M. Zhang*, X.L. Yao, X.B. Yu

School of Shipbuilding Engineering, Harbin Engineering University, Harbin 150001, China

Received 3 October 2007; accepted 3 October 2007
Available online 8 November 2007

Abstract

The fluid is assumed to be inviscid and incompressible and the flow irrotational. A time-integration boundary-integral method is used to solve the Laplace equation for the velocity potential to calculate the shape and position of the bubble. To improve the accuracy of the solution, the high-order triangular elements with curved sides and surfaces defined by six nodes are used to discretize the boundary surface in this investigation. Meanwhile, the singularity of the double-layer potential is eliminated by recasting the principal-value integral of the double-layer potential when the influence coefficient matrix is calculated. The material velocity vector at any node can be obtained by the potential of adjacent nodes with an appropriate weighted method. Elastic mesh technique (EMT), which is a new mesh regulation technique, is further applied to maintain the regularity of the triangular-element mesh used to discretize the dynamic boundary surface during the evolution of explosion bubble(s). All these efforts make the present approach viable and robust, and which is validated by computations of several bubble dynamics problems. Numerical analyses are carried out for the evolution of a bubble near a free surface and the interaction of two bubbles with a floating structure near a free surface. The robustness of the algorithm is demonstrated through simulating bubble jets near a free surface producing sharp free surface spikes and bubble(s) collapsing nearby a floating structure close to a free surface.

1. Introduction

During an underwater explosion, there will be a transient shock wave with high velocity and pressure propagating radially outwards to be followed by a large bubble containing hot gaseous products of the explosion [1–4]. Subsequent secondary shocks may be encountered with every time the bubble reaches a minimum volume. The shock wave has the first damaging effect on a nearby solid structure (e.g. ship, submarine, etc.), because of the very high pressures associated. The explosion products will then form a high-pressure gas bubble. Due to inertia, the bubble over-expands and the pressure inside decreases. Since the ambient pressure is now higher than that inside the bubble, which will cause the collapse of the bubble. If expansion and collapse occur near an underwater structure, under certain conditions, the bubble will create a high-speed re-entrant water jet towards the structure. This jet always originates on the farther side of the bubble with respect to the structure. The jet will penetrate the bubble and impact on the other bubble wall, creating a toroidal bubble. The pressure involved in this jetting process is not as high as the

*Corresponding author. Tel.: +86 451 82518954; fax: +86 451 82518296.
E-mail address: amanzhang@gmail.com (A.M. Zhang).

0022-460X/$ - see front matter © 2007 Elsevier Ltd. All rights reserved.
doi:10.1016/j.jsv.2007.10.007

pressure generated by the shock wave but with much longer duration. It is believed that the second damaging effect is created through this mechanism. In general, the physics associated with the shock waves are of the order of milliseconds, whereas the flow physics associated with the bubbles are of the order of seconds.

Boundary element method (BEM) is commonly applied in the simulation of bubble(s) dynamics and its inherent property of reducing the dimension of the problem by one can greatly save computational effort. This can become a critical issue in the simulation of three-dimensional (3D) multiple bubbles with more complex geometrical solid boundaries and/or free surface. The employment of BEM to bubble dynamics can be seen in the early work of Blake and Gibson [5,6] who studied the growth and collapse of vapor cavitation near a free surface. Their numerical results of the bubble shape as it evolved matched well with the experiment, which suggested that BEM can be a good approach to capture the complex features of bubble dynamics including the formation of water jet. Previous theoretical studies on bubble dynamics have tended to focus on cases of spherical and axisymmetric bubbles. It is only recently that researchers have begun to explore the simulation of 3D bubbles. However, most studies are based on linear plane boundary elements with three-node flat triangles. To improve solution accuracy, the boundary surface is discretized into six-node curved triangular elements in this paper. Meanwhile, the singularity of the double-layer potential is eliminated by recasting the principal-value integral of the double-layer potential when the influence coefficient matrix is calculated. The material velocity vector at any node can be obtained by the potential of adjacent nodes with an appropriate weighted method. Elastic mesh technique (EMT) is further applied to get the optimum velocity of each node. Therefore, even no smoothing algorithm has been applied and yet the results obtained are reasonably smooth for all the cases considered.

2. Theoretical background

Fig. 1 shows a schematic view of the problem to be discussed in this paper. We focus on the case of a pressure-driven gas bubble initiated near a rigid infinite wall in an incompressible fluid. In this work, surface tension effect was not taken into account because of the generally large size of the gas bubbles. Viscous effects are also neglected because the timescale for viscous diffusion is much larger than the oscillation period for these bubbles. In addition, a rectangular coordinate system O-xyz was adopted with the origin located at the center of the initial spherical bubble and the z-axis pointing in the opposite direction to gravity (Fig. 1). The boundary of the bubble is denoted as S_b, which is a regular surface before and after the jet impact. The fluid domain is denoted by Ω and it is transformed from a singly connected to a doubly connected region during jet impact.

In this paper, we assume that the bubbles only contain a non-condensable gas, which can be described as ideal and the expansion and compression of this gas as adiabatic [7,8]. The internal bubble pressure, P, as a

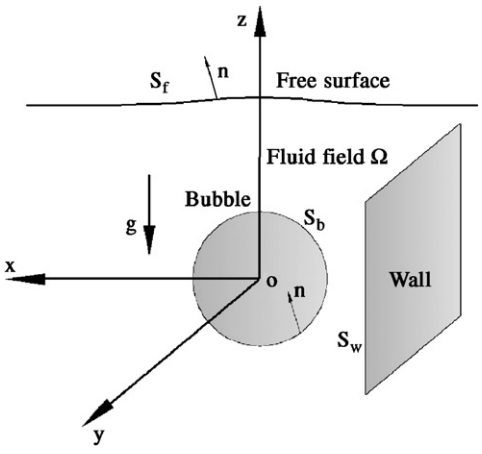

Fig. 1. Coordinate system.

function of the bubble volume, V, is

$$P = P_c + P_0(V_0/V)^{\gamma}, \tag{1}$$

where P_c is the constant vapor pressure inside the bubble. V_0 is the volume of the bubble at which the partial pressure due to the non-condensing gas would be P_0. γ is the ratio of specific heats, and $\gamma = 1.4$ for the ideal diatomic gas. We take $\gamma = 1.25$ [9] in this investigation. The fluid in the time-varying fluid domain Ω (Fig. 1) is assumed to be inviscid, incompressible and the flow irrotational. The velocity potential ϕ is governed by the Laplace equation:

$$\nabla^2\phi = 0. \tag{2}$$

The velocity, $\mathbf{u}$, anywhere in the flow can now be written as

$$\mathbf{u} = \nabla\phi. \tag{3}$$

2.1. Direct boundary element method

The Laplace equation is an elliptic equation, so the solution can always be computed everywhere in the fluid domain, provided that either the potential, ϕ (Dirichlet condition) or the normal velocity, $\partial\phi/\partial n$ (Neumann condition) is given on the boundaries of the problem. Here $\partial/\partial n = \mathbf{n}\cdot\nabla$ is the normal inward derivative from the boundary, S, and $\mathbf{n}$ is directed out of the fluid, applying the boundary condition at infinite distance '∞'

$$r = \sqrt{x^2 + y^2 + z^2} \to \infty, \quad \phi \to 0, \tag{4}$$

where $r = (x, y, z)$ is the position vector. The boundary-integral equation can be written as

$$\lambda\phi(\mathbf{p}) = \iint_S \left(\frac{\partial\phi(\mathbf{q})}{\partial n} G(\mathbf{p},\mathbf{q}) - \phi(\mathbf{q}) \frac{\partial}{\partial n} G(\mathbf{p},\mathbf{q}) \right) \mathrm{d}S. \tag{5}$$

Eq. (5) is Green's integral formula, where S is boundary surface including the bubble surface S_b, the free surface S_f, and the wall surface S_w; p and q are fixed particle and integral variable on boundary surface S, respectively; λ is the solid angle viewed from the point $\mathbf{p}$. $\lambda = 4\pi$ when the point $\mathbf{p}$ is located inside the flow field, $\lambda = 2\pi$ when the point $\mathbf{p}$ is located on the smooth boundary surface, and $\lambda < 4\pi$ when the point $\mathbf{p}$ is located on the corner. The solid angle subtended at the governing point $\mathbf{p}$ can be obtained through integral as follows:

$$\lambda = \iint_S \frac{\partial G}{\partial n}(\mathbf{p},\mathbf{q})\,\mathrm{d}S, \quad \mathbf{p} \in S, \tag{6}$$

$G(\mathbf{p}, \mathbf{q})$ is the free-space Green's function for the Laplace equation, which is governed by

$$G(\mathbf{p},\mathbf{q}) = |\mathbf{p} - \mathbf{q}|^{-1}. \tag{7}$$

2.2. Indirect boundary element method

Here we will use the same notations for Ω as the flow field and S as surface bounding the flow field as described in Section 2.1. The distributed source is arranged on the boundary surface with source density $\sigma(\mathbf{q})$, while r_{pq} is the distance between the fixed particle $\mathbf{p}$ and integral variable $\mathbf{q}$ on the surface S. If the point $\mathbf{p}$ is located inside Ω (not on S), then the total velocity potential and velocity at point $\mathbf{p}$ induced by all the sources distributed continuously on S can be evaluated by integration over S:

$$\phi(\mathbf{p}) = -\iint_S \frac{\sigma(\mathbf{q})}{r_{pq}}\,\mathrm{d}S_q, \tag{8}$$

$$\mathbf{u}(\mathbf{p}) = -\iint_S \frac{\sigma(\mathbf{q})\bar{r}(pq)}{r_{pq}^3}\,\mathrm{d}S_q. \tag{9}$$

If point **p** is located on S, Eqs. (8) and (9) cannot be applied directly as the associated integral points are singular. The detailed method can be referred to Refs. [10,11]. When the indirect boundary element method (IBEM) is adopted, source density $\sigma(\mathbf{q})$ is obtained through Eq. (8) with given boundary conditions. Induced velocity of each node on the surface S is solved with Eq. (9). In this paper, DBEM and IBEM are both employed to simulate the dynamics of underwater explosion bubble in the flow field.

2.3. Potential flow model

The surface tension is neglected in this investigation, for it is insufficient to cause appreciable effect for most of the lifetime of a cavitation or explosion bubble. The dynamics of the flow is driven by the pressure boundary condition: the pressure on the liquid side of the boundary surface, $P = P_b$, and the momentum conservation via the Bernoulli equation,

$$P = \rho g H - \rho \frac{\mathrm{D}\phi}{\mathrm{D}t} + \frac{1}{2}\rho|\mathbf{u}|^2, \tag{10}$$

where ρ is the fluid density and H is the initial bubble depth

$$\frac{\mathrm{D}\mathbf{x}}{\mathrm{D}t} = \mathbf{u}. \tag{11}$$

On a rigid wall, naught normal velocity has been applied as a boundary condition:

$$\nabla\phi \cdot \mathbf{n} = 0, \tag{12}$$

where $\mathbf{x}$ is the spatial position vector of fluid particles on the bubble surface and $\mathbf{n}$ is the normal vector of the boundary.

The maximum radius of the bubble is denoted by R_m. Gravity being ignored, R_m can be defined by Eq. (15). Pressure difference is defined as $\Delta P = P_\infty - P_c$, where ambient pressure of the flow field is $P_\infty = P_{\mathrm{atm}} + \rho g H$ at the depth H (initial position of the explosion center). The scaling factors are non-dimensional for length, pressure, time, velocity potential and buoyancy; chosen to be R_m, ΔP, $R_m(\rho/\Delta P)^{1/2}$, $R_m(\Delta P/\rho)^{1/2}$, and $(\rho g R_m/\Delta p)^{1/2}$, respectively. Slash $'$ is added on the original variables to distinguish them. Eq. (10) in non-dimensional form is

$$\frac{\mathrm{D}\phi'}{\mathrm{D}t'} = 1 - \varepsilon\left(V_0'/V'\right)^{\gamma} - \delta^2 z' + \frac{1}{2}|\mathbf{u}'|^2 \quad (\text{on } S_b), \tag{13a}$$

$$\frac{\mathrm{D}\phi'}{\mathrm{D}t'} = \frac{1}{2}\left|\mathbf{u}'\right|^2 - \delta^2(z' - \gamma_f) \quad (\text{on } S_f), \tag{13b}$$

$$\frac{\mathrm{D}\phi'}{\mathrm{D}t'} = 1 - P' - \delta^2 z' + \frac{1}{2}|\mathbf{u}'|^2 \quad (\text{on } S_w), \tag{13c}$$

where $\delta = (\rho g R_m/\Delta P)^{1/2}$, $\varepsilon = P_0/\Delta P$,$\gamma_f = d/R_m$, d is the initial position of the bubble center.

The dimensionless parameter ε defines the ratio between bubble's initial gas pressure just after explosion and the hydrostatic pressure at explosion center. Redefine Eq. (11) into non-dimensional form as

$$\frac{\mathrm{D}\mathbf{x}'}{\mathrm{D}t'} = \mathbf{u}'. \tag{14}$$

At initial condition $\phi' = 0$ at $t' = 0$. Eqs. (5), (13) and (14) form a complete set of equations which describes the evolution of the bubble(s) for all the cases considered.

2.4. Toroidal bubble

After the jet penetrates the bubble, the bubble becomes toroidal and the flow field becomes doubly connected. The velocity potential function ϕ may be multi-valued and new or revised computational procedures are required. To date, there have been a few studies for axis-symmetrical toroidal bubbles. Lundgren and Mansour [12] formulated a physically motivated model by representing the solution using a

smooth dipole distribution over the bubble surface, together with a singular vortex ring localized within the bubble. Their model is only suitable for a bubble with a constant volume. Best [13] introduced a contiguous branch cut and formulated the boundary-integral equation both on the bubble surface and on the cut. The cut needs special numerical treatment. Zhang et al. [14] and Zhang and Duncan [15] presented a hyper singular boundary-integral method for toroidal bubbles. In their computation, a layer was defined to separate the water jet and the surrounding domain during the toroidal bubble phase. This layer acts as a vorticity sheet and moves with the flow. The layer deforms as much, if not much more than the bubble surface, which can make the tracking very challenging. Wang et al. [7,8] employed a so-called surgical-cut to convert the originally simply connected bubble to a toroidal shape after the jet impact. Instead of adding a vortex sheet at the impact area, a vortex ring was placed inside the bubble to account for the double connectivity of the bubble. There is no longer the need for meticulous tracking of the vorticity sheet as in Zhang et al. [14]; we just ensure that the vortex ring stays inside the toroid as the bubble evolves. Zhang et al. [1] extended the surgical-cut and vortex ring technique to general 3D toroidal bubble problems, looking specifically at the issues of the physical impact and its relation to the numerical stability of the BEM code.

3. Initial conditions

For an explosive, the charge weight (W as expressed in kg) and the depth at which it explodes (H as expressed in m) are generally known. The relationship between these two parameters and the initial radius for the numerical calculations (R_0) and the maximum bubble radius (R_m) will be established now. At the same time an expression for the initial gas pressure inside the bubble just after the explosion P_0 will be obtained. For a TNT-charge, an empirical relationship between W, H and R_m exists [10] and given as

$$R_m = 3.38\left(\frac{W}{H+10}\right)^{1/3}. \tag{15}$$

The maximum volume of the bubble will thus be linearly dependent on the charge weight and inversely proportional to the hydrostatic pressure. Another empirical relationship for the initial pressure of the explosion products (TNT-explosives) is

$$P_0 = 1.39\times 10^5 (W/V_0)^{\gamma}. \tag{16}$$

For spherically symmetrical bubbles, the Rayleigh–Plesset equation can be used as an equation of motion (written in dimensionless form):

$$\ddot{R}'R' + 1.5\dot{R}'^2 = \varepsilon(R_0'/R')^{3\gamma} - 1. \tag{17}$$

Here R' is the dimensionless radius of the bubble. The relationship between the bubble initial radius R_0, the weight of the explosive charge W and the bubble maximum radius R_m can be obtained from simultaneous system of Eqs. (15)–(17) and Eq. (1):

$$\frac{1.39\times 10^5}{\Delta P}\frac{1}{(\gamma-1)}\left(\frac{3W}{4\pi R_m^3}\right)^{\gamma}\left[1-\left(\frac{R_0}{R_m}\right)^{-3(\gamma-1)}\right] = \left(\frac{R_0}{R_m}\right)^3 - 1. \tag{18}$$

The bubble initial radius R_0 can be calculated because R_0 is the only unknown quantity while the other parameters are all known in Eq. (18). For example, a 1000 kg TNT explosion at a depth of 60 m gives rise to a maximum bubble radius $R_m = 8.2$ m, the initial pressure $P_0 = 1.01\times 10^8$ Pa and the reference pressure $\Delta P = 7.06\times 10^5$ Pa. The dimensionless parameters for this case are $\gamma = 1.25$, $R_0' = 0.1304$, $\varepsilon = 143.6$, $\delta^2 = 0.1167$ and the time scale is $\Delta t = 0.3126$ s.

4. Numerical solutions

The high-order curved triangular elements are used to discretize the bubble surface in this paper, as illustrated in Fig. 2(a). To describe the surface of an element in parametric form, we map each curved triangle in physical 3D space to the familiar right isosceles triangle in the $\xi\eta$ plane, as illustrated in Fig. 2(b). The first

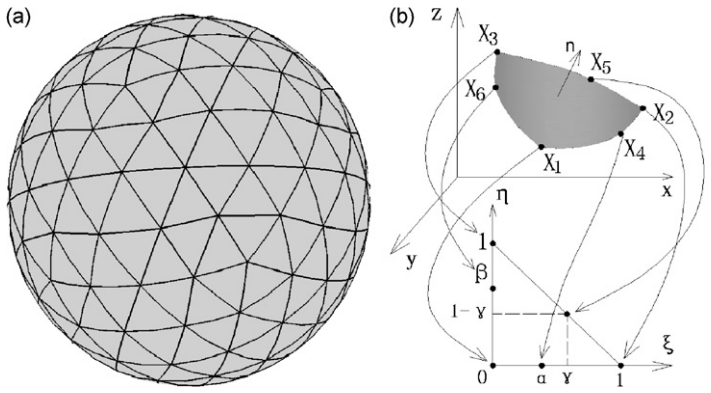

Fig. 2. The discretized bubble surface and the coordinate mapping: (a) the six-node curved element discrete surface and (b) a curved six-node triangle in three-dimensional space is mapped to a right isosceles triangle in the $\xi\eta$ plane.

element node is mapped to the origin, the second is mapped to the point $\xi = 1$, $\eta = 0$ on the ξ-axis, the third is mapped to the point $\xi = 0$, $\eta = 1$ on the η-axis, the fourth is mapped to the point $\xi = \alpha$, $\eta = 0$, the fifth is mapped to the point $\xi = \gamma$, $\eta = 1-\gamma$, and the sixth is mapped to the point $\xi = 0$, $\eta = \beta$.

Where $\varphi(\xi, \eta)$ are element-node cardinal interpolation functions defined as

$$\varphi_1 = 1 - \varphi_2 - \varphi_3 - \varphi_4 - \varphi_5 - \varphi_6, \tag{19}$$

$$\varphi_2 = \frac{1}{1-\alpha}\xi\left(\xi - \alpha - \frac{\alpha-\gamma}{1-\gamma}\eta\right), \tag{20a}$$

$$\varphi_3 = \frac{1}{1-\beta}\eta\left(\eta - \beta - \frac{\beta+\gamma-1}{\gamma}\xi\right), \tag{20b}$$

$$\varphi_4 = \frac{1}{\alpha(1-\alpha)}\xi(1-\xi-\eta), \tag{20c}$$

$$\varphi_5 = \frac{1}{\gamma(1-\gamma)}\xi\eta, \tag{20d}$$

$$\varphi_6 = \frac{1}{\beta(1-\beta)}\eta(1-\xi-\eta), \tag{20e}$$

$$\alpha = \frac{1}{1+\left|\dfrac{X_4 - X_2}{X_4 - X_1}\right|}, \quad \beta = \frac{1}{1+\left|\dfrac{X_6 - X_3}{X_6 - X_1}\right|}, \quad \gamma = \frac{1}{1+\left|\dfrac{X_5 - X_2}{X_5 - X_3}\right|}. \tag{20f}$$

The bubble surface S is discretized into a set of N nodal points $P_i (i = 1, \ldots, N)$ and M triangular elements $\Delta_j (j = 1, \ldots, M)$. Here interpolation formula of every element is

$$\phi = \sum_{i=1}^{6} \varphi_i \phi_i, \quad \frac{\partial\phi}{\partial n} = \sum_{i=1}^{6} \varphi_i \frac{\partial\phi}{\partial n_i}, \quad \mathbf{x} = \sum_{i=1}^{6} \mathbf{x}_i \varphi_i(\xi, \eta), \tag{21}$$

where $\boldsymbol{x}$, ϕ and $\partial\phi/\partial n$ are nodal displacement vector, velocity potential and normal velocity, respectively, φ_i is the interpolation function. Then calculate the integral of every element to constitute the linear equation set which can be solved finally:

$$\left(\sum_{j=1}^{N} A_{ij} - \lambda_i \delta_{ij}\right)\phi_i = \sum_{j=1}^{N} B_{ij}\partial\phi_j/\partial n \Rightarrow \mathbf{H}\cdot\phi = \mathbf{G}\cdot\frac{\partial\phi}{\partial n}, \tag{22}$$

Table 1
Errors of calculating $\mathbf{H}_{ii}$

Number of nodes	42	162	640
Relative error (%)	6.3	0.9	0.1

A_{ij} and B_{ij} are the influence coefficients, $\mathbf{H}$ and $\mathbf{G}$ are the influence coefficient matrices and δ_{ij} is the Kronecker δ.

The non-diagonal elements of the influence coefficient matrix are calculated with a seven-point quadrature for triangles [16]. While the diagonal elements $\mathbf{G}_{ii}$ of the influence coefficient matrix are singular, the coordinate system should be converted into polar coordinate system for the integral to eliminate the singularity, referring to Ref. [17]. When computing $\mathbf{H}_{ii}$, the general algorithm [18] is adopted as shown by Eq. (23), but there is an error in every time step with this method, as shown in Table 1

$$\mathbf{H}_{ii} = 4\pi - \sum_{\substack{j=0 \\ i\neq j}}^{N} \mathbf{H}_{ij}. \tag{23}$$

From Table 1, it can be seen that although the error can be reduced by adding nodes, accumulated error will be generated with the increment of time step, which will result in the instability in calculation process. In order to eliminate this error, the paper is based on the method described in Ref. [19]. Consider a singly or multiply connected control volume, denoted by V_s, and bounded by a closed surface or a collection of closed surfaces, denoted by S. The boundary associated with the Green's function may be one of these surfaces. For the moment, using the divergence theorem and the distinctive properties of the delta function in three dimensions, we find that the Green's functions satisfy the integral identity

$$\int_S \frac{\partial}{\partial n} G(\mathbf{p},\mathbf{q})\,\mathrm{d}S(\mathbf{p}) = \begin{cases} 4\pi & \text{when } \mathbf{q} \text{ is inside } V_s, \\ 2\pi & \text{when } \mathbf{q} \text{ is on } S, \\ 0 & \text{when } \mathbf{q} \text{ is outside } V_s, \end{cases} \tag{24}$$

where the unit normal vector $\mathbf{n}$ points into the control volume V_s. When the point $\mathbf{q}$ is located on the boundary S, the improper integral on the left-hand side of Eq. (24) is a principal-value integral.

Using the three relations shown in Eq. (24), the integral formula can be obtained by recasting the principal-value of the double-layer potential:

$$\int_S^{PV} \phi(\mathbf{p}) \left[\frac{\partial}{\partial n} G(\mathbf{p},\mathbf{q})\right] \mathrm{d}S(p) = \int_S [\phi(\mathbf{p}) - \phi(\mathbf{q})] \left[\frac{\partial}{\partial n} G(\mathbf{p},\mathbf{q})\right] \mathrm{d}S(\mathbf{p}) + 2\pi\phi(\mathbf{q}). \tag{25}$$

Using Taylor series expansions on Eq. (25), it is found out that as the integration point $\mathbf{p}$ approaches the evaluation point $\mathbf{q}$, the integrand on the right-hand side is non-singular, i.e. the singularity of $\mathbf{H}_{ii}$ is eliminated using the integral formula by recasting the principal-value integral of the double-layer potential. Eqs. (24) and (25) can only be applied for a closed surface, and for the problems with open surface, it can be dealt with by connecting the surface into closed regions artificially.

The physical state of the dynamical problem is fully specified when the position of the boundary S and the distribution of velocity potential ϕ on it are known. With these, the tangential velocity vector along the boundary S can be evaluated. The normal velocity component $\partial\phi/\partial n$ may be determined from the boundary-integral formula (5) by treating it according to Eqs. (22)–(25). With $\nabla\phi$ on the boundary S being known, Eqs. (13) and (14) may be numerically integrated in time to find the new position of the boundary S with a corresponding new distribution of ϕ on it. The forward time integration of Eqs. (13) and (14) is carried out using the predictor-corrector scheme. To maintain the stability of the solution, the time-step size Δt must be carefully controlled so that the changes in the potential are bounded at each time step. In the present paper the

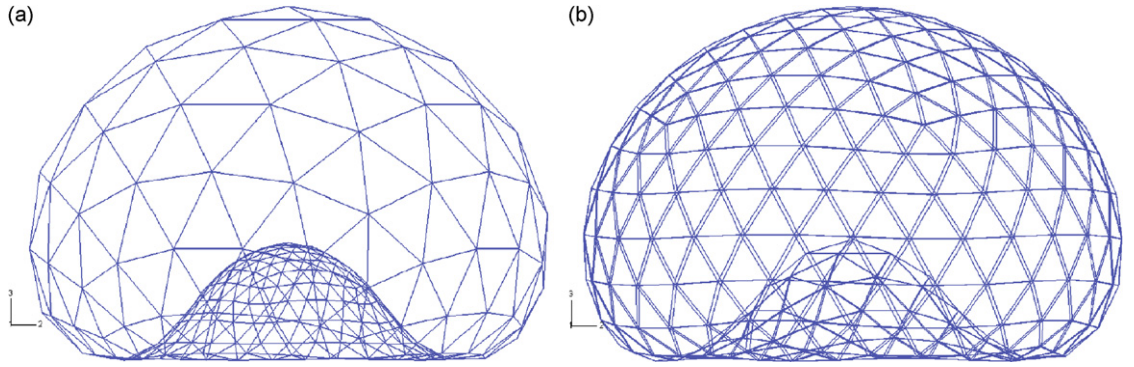

Fig. 3. Mesh advanced using material velocity and EMT optimum velocity: (a) mesh advanced using material velocity and (b) mesh advanced using EMT optimum velocity.

time-step size Δt is chosen as

$$\Delta t = \frac{\Delta\phi}{\max\left|1 + \frac{1}{2}\left|\nabla\phi\right|^2 - \delta^2 z - \varepsilon(V_0/V)^{\gamma}\right|}, \tag{26}$$

where $\Delta\phi$ is some constant. With this choice of Δt, the change in ϕ at each node is bounded above by $\Delta\phi$. The results in this work are obtained with $\Delta\phi$ kept to around 0.01.

5. Elastic mesh techniques

In the simulation of bubble dynamics with jet formation, the jet tip exhibits strong sink characteristic. The elements on the bubble surface tend to converge fairly rapidly towards the jet tip and quickly become over crowded in the jet tip vicinity. (Strictly, the inherent presence of more elements for better resolution of the jet is a reasonable and acceptable development. The objection arises when too many elements are in the jet tip vicinity which results in thinning out the element distribution in other regions.) This accumulated imbalance of element distribution will eventually lead to the early breakdown of the simulation in the absence of other interventions. In order to make the element distribution as reasonably uniform as possible, EMT is introduced. EMT is based on the idea that if the mesh is made of elastic ribbons, it should be able to automatically adjust its shape optimally: all segment lengths are close to equal. In essence, the optimum mesh is found by minimizing the total elastic energy stored in each segment of the mesh. This approach has an advantage that it actively seeks in a forward manner the optimum mesh for computation at each time step. This is quite different from those where the re-distribution takes place after the calculations are made. Compared with the conventional node insertion and deletion approach, EMT keeps the number of nodes and topological structure of the mesh unchanged. (This may become a critical issue in deriving an efficient algorithm for matrix inversion in the simulation of multiple bubbles with complex geometric and yet the number of elements is kept constant without the additional complexities of mesh refinement and deletion.) Instead of advancing by the material velocity, EMT produces an optimum mesh shifting velocity, which ensures the regularity of the mesh after advancement (see Fig. 3). Wang et al. [20] are found that EMT has enabled a much more even distribution of the meshes representing the bubble surface even in the midst of a strong jet formation where there is great difference in the surface velocity of the bubble. In doing so, the incorporation of EMT has permitted the use of significantly larger time stepping and still within reasonable accuracy.

6. Numerical results and discussion

6.1. Dynamics of one bubble in an unbounded fluid

One of the simplest bubble dynamics problems is the Rayleigh bubble. There exists a simple ordinary differential equation (ODE) describing its behavior, which can be solved accurately by standard ODE solver

such as the fourth-order Runge–Kutta method. The Rayleigh bubble calculated here has initial radius $R_0 = 0.1304$ and pressure $\varepsilon = 143.6$ and $\delta = 0$. The initial spherical bubble surface is discretized into a set of 320 six-node curved triangular elements. Since in this case the bubble is expanding and collapsing uniformly and so is the mesh distribution kept uniform, no mesh optimization via EMT is applied. Comparisons of results by IBEM, DBEM and the direct solution of Rayleigh equation about the radius variation over two cycles of the evolution including the expansion phase and collapse phase for Rayleigh bubble have been carried out in Fig. 4, which show great agreement with each other. Fig. 4 also shows that the solution of DBEM is nearly in superposition with that of IBEM. So in the next section of this paper, DBEM is adopted to solve bubble dynamics problems.

Theoretically, Rayleigh bubble will keep spherical throughout its whole lifetime, i.e. the radius at all surface points should be identical. In order to evaluate the influence of numerical errors on the deformation of the Rayleigh bubble, the maximum absolute deviation of the bubble surface from the spherical Rayleigh's bubble is also shown in Fig. 4. The error increases when the bubble is around its minimum volume but the error line relatively flat otherwise. It is implied that the Rayleigh bubble is most unstable at its minimum size. Generally, the error line indicates a mild increasing trend as the numerical errors are constantly accumulating during the computations. Besides, the time history of pressure inside the bubble is shown in Fig. 5.

To verify the advantage of the six-node curved triangular elements adopted in this paper and the plane triangular elements adopted by Wang and Khoo [10], the initial bubble is discretized into 162 six-node curved triangular elements and three-node plane triangular elements, respectively, and the motion cycles are simulated separately. The time history of the Rayleigh bubble volume calculated is shown in Fig. 6.

Fig. 6 shows that the bubble volume variation solved by curved triangular elements is in excellent agreement with the exact solution. However, greater error is induced by plane triangular elements compared with the

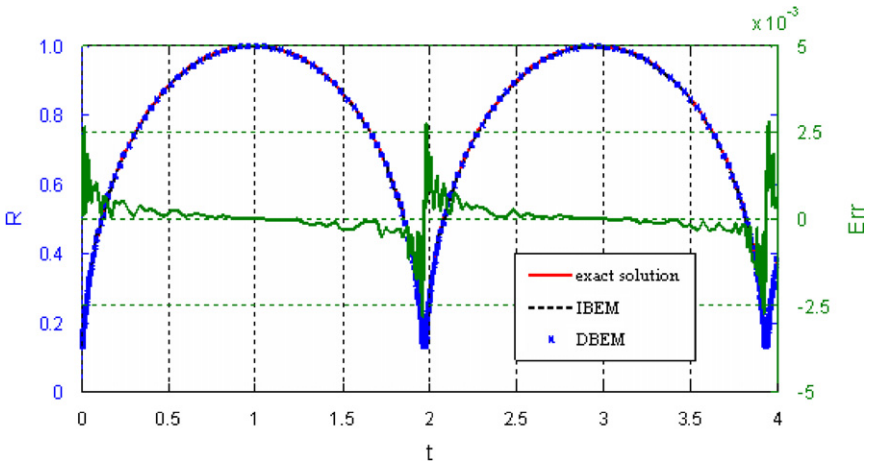

Fig. 4. The time history of the Rayleigh bubble radius calculated from the Rayleigh–Plesset equation using a fourth-order Runge–Kutta method (solid line), the 3D model using the present approach with IBEM (dash line), DBEM nodes (dots) being used.

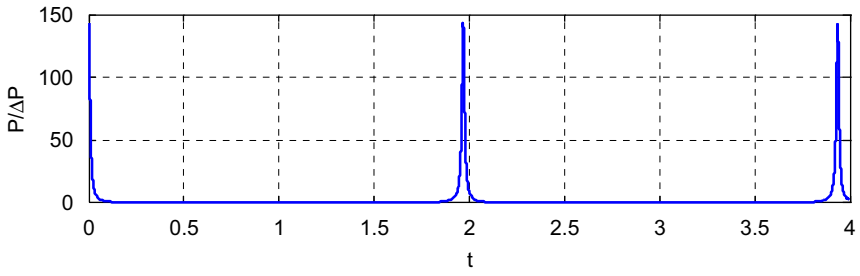

Fig. 5. The time history of pressure inside the bubble.

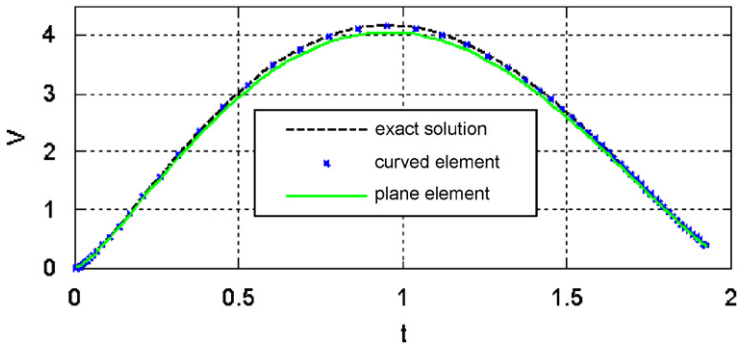

Fig. 6. The time history of the Rayleigh bubble volume calculated from the Rayleigh–Plesset equation using a fourth-order Runge–Kutta method (dash line), the 3D model using the present approach with three-node plane triangular element (solid line), six-node curved triangular element (dots) being used.

exact solution, which indicates that the bubble behavior simulated by curved elements is of higher accuracy than the simulation by plane elements with the same nodes. Furthermore, the curved elements can be employed to efficiently simulate complex curved boundary, such as free surface and structure boundary with great curvature, etc.

6.2. Dynamics of one bubble near a free surface

In this case, both the gravity and free surface effects are taken into account, with the initial size and pressure ($R_0 = 0.09$ and pressure $\varepsilon = 408.6$) is located 0.8 dimensionless units under the initially quiescent free surface. The gravity is in the vertical direction with strength $\delta^2 = 0.57$. The initial bubble is discretized into 320 six-node curved triangular elements, while the free surface with a non-dimensional size of 6×6 units is discretized into 690 six-node curved triangular elements. The source distribution outside the surface mesh area is assumed to be null value. EMT is applied to maintain the regularity of the triangular-element mesh used to discretize the dynamic boundary surface during the evolution of explosion bubble.

Fig. 7(a) shows the initial configuration. (On these figures, the color contour represents the magnitude of the potential function, ϕ.) At time $t = 0.29$ the bubble is in its expanding phase and there can be found a small rise on the free surface (Fig. 7(b)). During the expanding phase, the gravity and the Bjerknes [21] repellent from the free surface show little influence on the bubble behavior. When the bubble reaches its maximum size, it is still kept nearly spherical. The maximum bubble size is reached when $t = 0.69$ which is displayed in Fig. 7(c). Some deformation of the bubble shape can be observed at this time. On the free surface, a higher rise is achieved and obvious surface peak attributing to the presence of the bubble is observed. After reaching its maximum size, the bubble starts to collapse. In the consequent collapsing phase, the effect of gravity is felt. The lower bubble boundary moves faster than the upper one which makes the bubble become a bean-like shape at non-dimensional time of $t = 1.19$ and the start of jet formation process (Fig. 7(d)). In Fig. 7(e) the jet is fully developed and going to impact the upper boundary of the bubble. At the dimensionless time of 1.38 (Fig. 7(f)), the jet has impacted on the opposite bubble surface and a toroidal bubble is formed via the employment of a surgical-cut and a vortex ring. The purple bar inside the toroidal bubble is the vortex ring placed to simulate the rotational part of the flow. Fig. 7(g) shows the further evolution of the toroidal bubble which is in the process of rebounding. Correspondingly, there is a jet on the free surface pointing upwards.

It may be noted that EMT was applied in both the simulations of Fig. 7 which serves to avoid the overcrowding of elements in the jet tip vicinity. EMT works well throughout the phase of the toroidal bubble evolution. Had EMT not been employed, there would have been necessary to employ nodes insertion to avoid exceedingly large size elements and mesh refinements at other parts so that the shape of the bubble is still reasonably smoothed. The present results have also been compared with those of a validated axis-symmetrical bubble model [7,8] for a axis-symmetrical case. The results of the axis-symmetrical method are shown in Fig. 8. Fig. 9 shows that the present results compare favorably with those from an axisymmetric model.

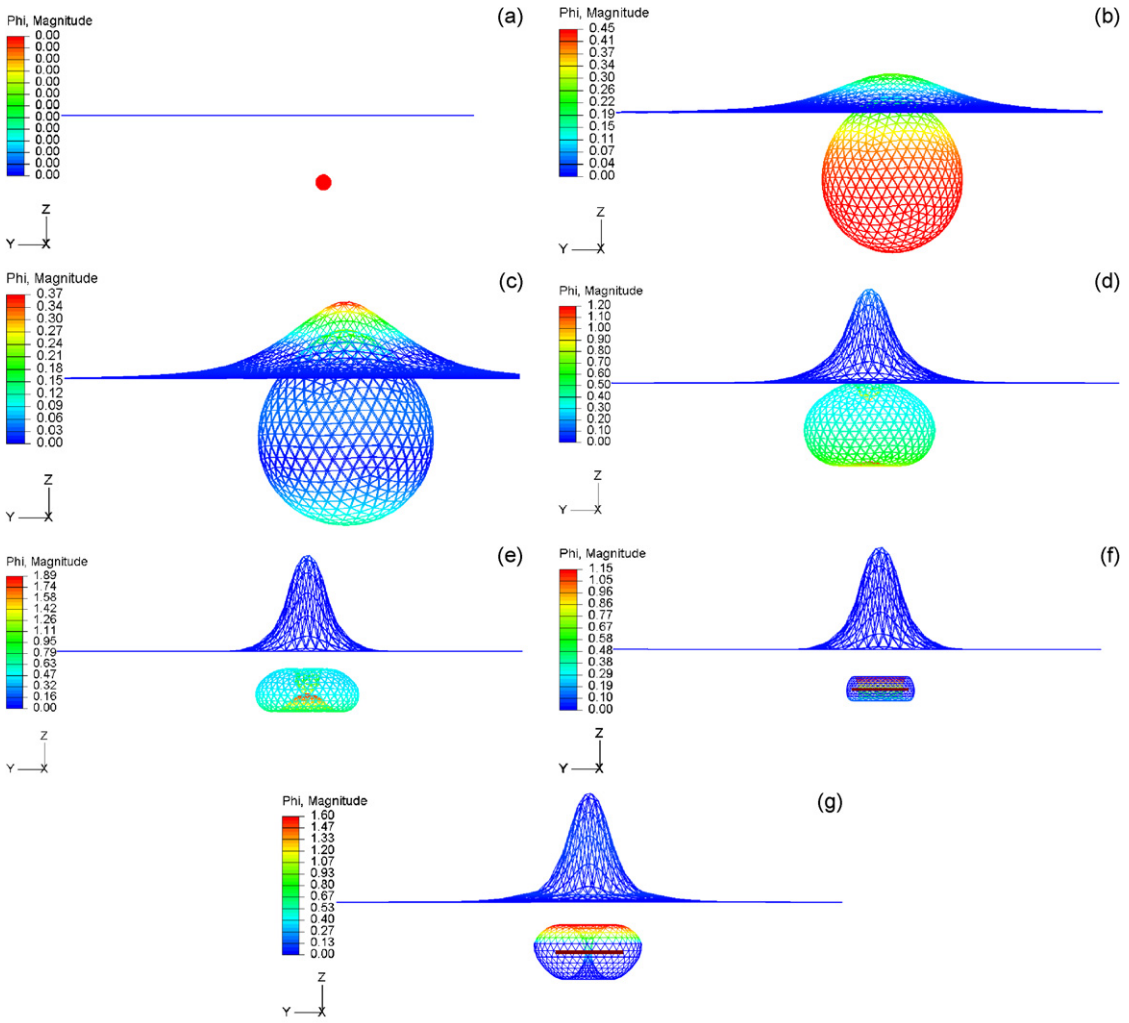

Fig. 7. Evolution of one bubble near a free surface ($\varepsilon = 408.6$ and $\delta^2 = 0.57$): time (a) $t = 0.00$, (b) $t = 0.29$, (c) $t = 0.69$, (d) $t = 1.19$, (e) $t = 1.32$, (f) $t = 1.38$, and (g) $t = 1.49$.

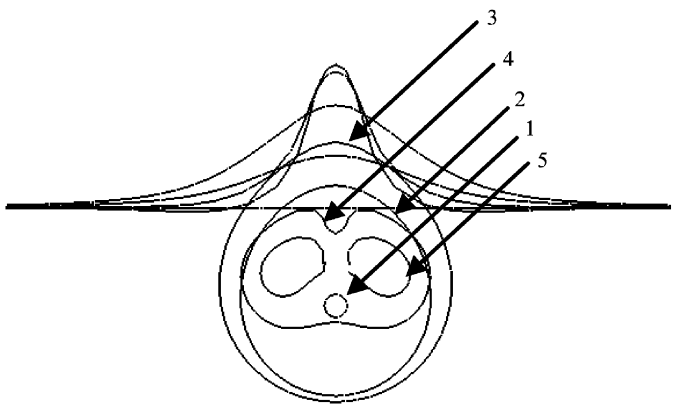

Fig. 8. Evolution of one bubble near a free surface using axisymmetric model ($\varepsilon = 408.6$ and $\delta^2 = 0.57$): time (1) $t = 0.00$, (2) $t = 0.29$, (3) $t = 0.69$, (4) $t = 1.19$, and (5) $t = 1.35$.

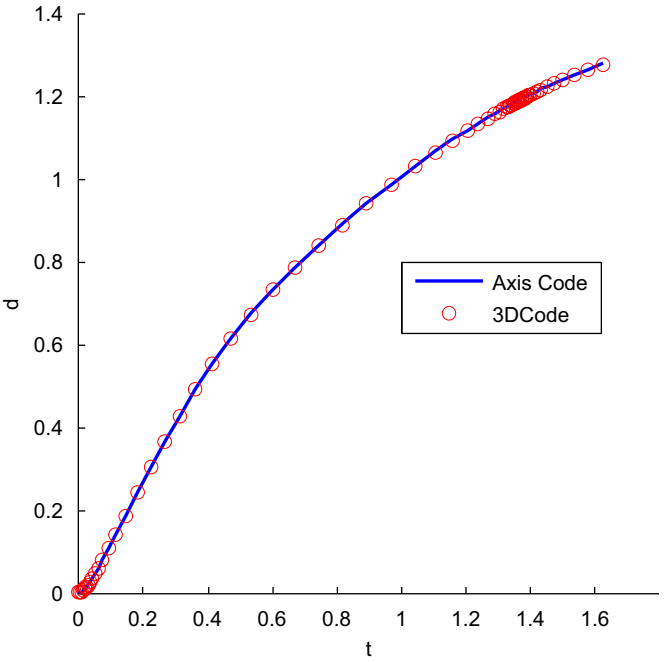

Fig. 9. The time history of the free surface peak vertical displacement using axisymmetric model (dash line), the 3D model (dots) in this paper.

6.3. *Dynamics of one bubble near a floating cylinder under free surface*

This case studies the evolution of one explosion bubble near a rigid cylinder (see Fig. 10(a)) in the presence of the free surface. The explosion bubble is originally spherical the same as the case in Section 6.2. The cylinder is located to the right side of the bubble at a distance of 0.7 dimensionless units. The radius and length of the rigid cylinder are 1 dimensionless unit and 6 dimensionless units, respectively. The initial free-surface is located 0.8 units above the bubble center. The initial bubble is still discretized into 320 six-node curved triangular elements and the free surface with the cylinder is discretized into 1680 six-node curved triangular elements. The calculating results are given out in the dimensionless form as shown in Fig. 10.

Fig. 10(a) shows the initial configuration. (On these figures, the color contour represents the magnitude of the potential function, ϕ.) During the expanding phase gravity shows little influence on the bubble behavior. The bubble continues to expand till its maximum size at time 0.68 in Fig. 10(b). Its shape is a little different from that of the same time in Section 6.2. One can easily detect the asymmetrical shape of the bubble with the surface facing the rigid cylinder exhibiting a flatter feature. There is an obvious rise of the free surface due to the expanding bubble. As time progresses, the bubble starts to contract and a jet pointing downwards is developed during the collapsing phase. At time 1.31, the jet is quite developed which is clearly observed in Fig. 10(d). The presence of the jet is manifested as higher pressure exerted on the left side of the rigid cylinder nearest the bubble. Because of the jet, the rise of the free-surface becomes even higher although the lateral extent has become smaller. The jet has impacted on the opposite bubble surface and a toroidal bubble is formed, and radiates pressure waves outwards. Then the time history of the pressure on some typical element of the cylindrical surface is shown in Fig. 11. Numerical analyses show that an underwater bubble placed near a structure (e.g. ship, submarine, etc.), will, in many cases, develop a jet directed towards this structure. This jet can be very powerful and is capable of destroying the ship (typical jet velocities can be 100 m/s or larger). Depending on the exact location of the bubble, the proximity to the free surface and the influence of gravity, the jet may impact on the structure or miss it completely. Therefore a thorough knowledge of the bubble dynamics can mean the difference between the survival or destruction of the structure.

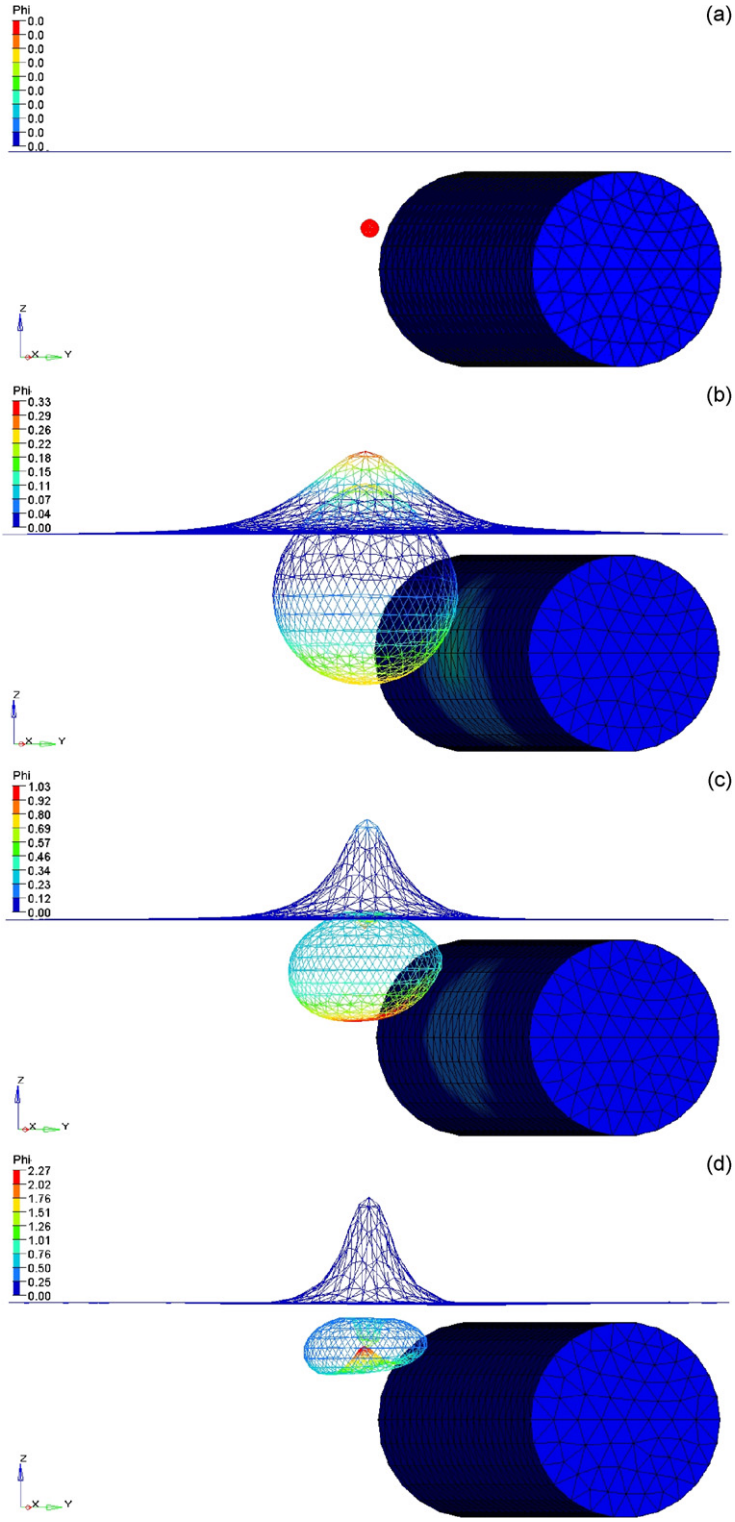

Fig. 10. Evolution of one bubble near a floating cylinder under free surface ($\varepsilon = 408.6$ and $\delta^2 = 0.57$): time (a) $t = 0.00$, (b) $t = 0.68$, (c) $t = 1.13$, and (d) $t = 1.31$.

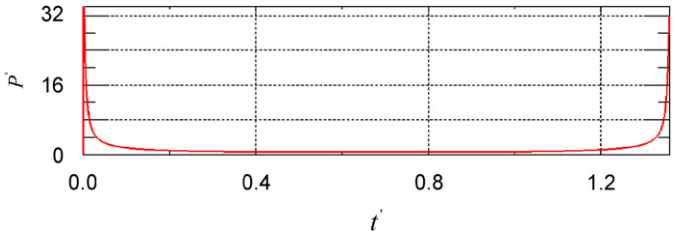

Fig. 11. The time history of the pressure on the cylinder surface.

Fig. 11 shows that the pressure peak is approximately 32 times of the atmospheric pressure. One pressure peak appears at the beginning of bubble expanding phase and another pressure peak in the final stage of bubble collapsing, which is called the second pulsation pressure. The second pulsation pressure makes the structure oscillating, and thereby causes serious overall structure damage. Because the residual energy inside the bubble is only 7 percent of the initial energy after the first bubble pulsation [9], so only the first bubble pulsation is considered to have made damage on the structure.

6.4. Dynamics of two bubbles near a floating cylinder under free surface

In the fourth case, the dynamics of two bubbles near a floating cylinder under free surface is investigated, which form a complete three-dimension problem. Single bubble is replaced with two bubbles with the same initial size and pressure placed along the axis of the cylinder and detonated synchronously based on Section 6.3. The horizontal distance between two bubbles is two dimensionless units. Each initial bubble is still discretized into 320 six-node curved triangular elements and the free surface with the cylinder is discretized into 1680 six-node curved triangular elements. The calculating results are given out in the dimensionless form as shown in Fig. 12.

Fig. 12(a) shows the initial configuration. (On these figures, the color contour represents the magnitude of the potential function, ϕ.) At the time of 0.68 (Fig. 12(b)), the bubble has about expanded to its maximum size. Some deformation of the bubble shape can be observed at this time, and because of the presence of the rigid cylinder and the free surface, their right sides are clearly flattened. On the free surface, a higher rise is achieved and obvious surface peaks attributing to the presence of the two bubbles are observed. After reaching its maximum size, the two bubbles are in the process of collapsing. At around $t = 1.13$ the two bubbles collapse further which is depicted in Fig. 12(c). Due to the effect of gravity, the bubble starts to lose its symmetry. In the numerical model, a water jet can be observed to develop from the right side of the bubble surface. At time $t = 1.35$, the oblique jets are formed, which are shown in Fig. 12(d). Another view is shown in Fig. 13. Correspondingly, there are two jets on the free surface pointing upwards.

7. Conclusions

In this paper, a 3D BEM approach is presented to study underwater explosion bubble problems. The dynamics of bubble(s) in four different arrangements have been simulated. For the simplest Rayleigh bubble case strict comparison is made with the analytical solution of Rayleigh equation, and there is very good agreement. Consider the effects of gravity on the bubble behavior, and numerical analyses are carried out for the evolution of a bubble near a free surface and the interaction of two bubbles and a floating structure near a free surface. No smoothing algorithm has been applied and yet the results obtained are reasonably smooth for all the cases considered, which suggests that the present approach proposed is stable and robust.

When the influence coefficient matrix is calculated, the singularity of the double-layer potential is eliminated by recasting the principal-value integral of the double-layer potential to improve the solution accuracy. Meanwhile, the solution accuracy can be further improved with high-order curved triangular elements without increasing the computation cost for the matrix is of full rank. When the normal and tangential velocities of the boundary surface are calculated, high-order curved elements show superiority in the processing methods employed such as interpolation, fit technique.

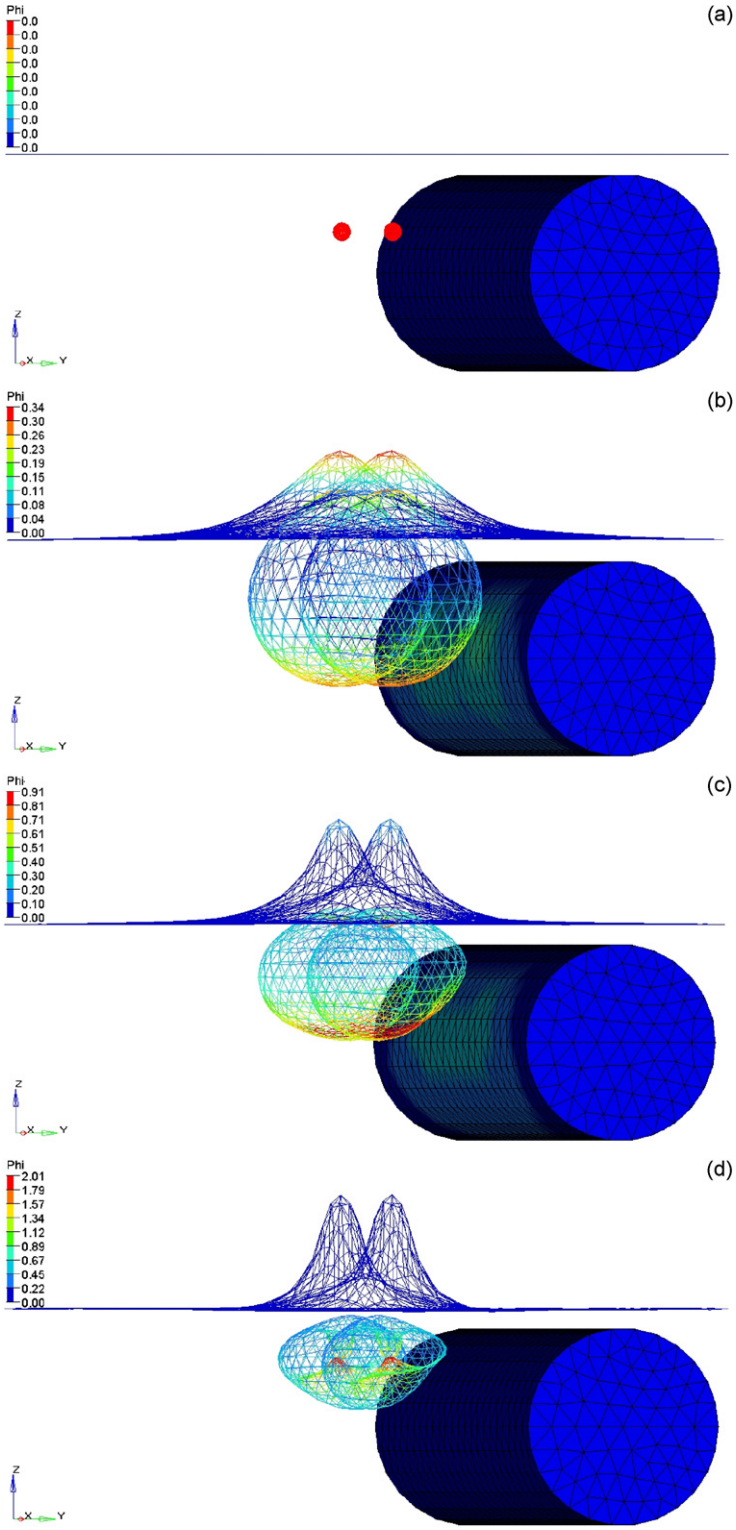

Fig. 12. Evolution of two bubbles near a floating cylinder under free surface ($\varepsilon = 408.6$ and $\delta^2 = 0.57$): time (a) $t = 0.00$, (b) $t = 0.68$, (c) $t = 1.13$, and (d) $t = 1.35$.

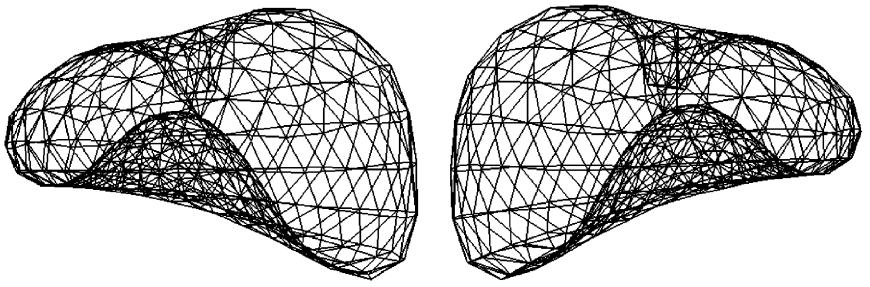

Fig. 13. The jet is formed during the bubbles collapsing.

During the expanding phase gravity shows little influence on the bubble behavior. When the bubble reaches its maximum size, it is still kept nearly spherical. In the consequent collapsing phase, the effect of gravity is felt, and the jet impacts on the opposite bubble surface and a toroidal bubble is formed. The presence of free surface, structure and gravity effect can give rise to jet(s) formation during the bubble(s) evolution. It is interesting to note their characteristics and differences. The free surface-induced jet always points downwards; while the gravity-induced jet always points upward and is not as sharp as the jet due to another bubble.

Numerical analyses show that an underwater bubble placed near a structure (e.g. ship, submarine, etc.), will, in many cases, develop a jet directed towards this structure. This jet can be very powerful and is capable of destroying the ship. Depending on the exact location of the bubble, the proximity to the free surface and the influence of gravity, the jet may impact on the structure or miss it completely. Therefore a thorough knowledge of the bubble dynamics can mean the difference between the survival or destruction of the structure.

Acknowledgment

This research is supported by a Grant (50779007/E0902) from the National Science Foundation of China.

References

[1] Y.L. Zhang, K.S. Yeo, B.C. Khoo, C. Wang, 3D jet impact and toroidal bubbles, *Journal of Computational Physics* 166 (2) (2001) 336–360.
[2] S. Rungsiyaphornrat, E. Klaseboer, B.C. Khoo, K.S. Yeo, The merging of two gaseous bubbles with an application to underwater explosions, *Computers & Fluids* 32 (1) (2003) 1049–1074.
[3] A.H. Keil, The response of ships to underwater explosions, *Transaction of Society of Naval Architecture and Marine Engineering*, 1961.
[4] A.H. Keil, Introduction to Underwater Explosion Research, Norfolk Naval Ship Yard, Portsmouth, VA, 1956.
[5] J.R. Blake, D.C. Gibson, Growth and collapse of a vapour cavity near a free surface, *Journal of Fluid Mechanics* 111 (3–5) (1981) 123–140.
[6] J.R. Blake, D.C. Gibson, Cavitation bubbles near boundaries, *Journal of Fluid Mechanics* 19 (1) (1987) 99–123.
[7] Q.X. Wang, K.S. Yeo, B.C. Khoo, K.Y. Lam, Strong interaction between a buoyancy bubble and a free surface, *Theoretical and Computational Fluid Dynamics* 8 (5) (1996) 73–88.
[8] Q.X. Wang, K.S. Yeo, B.C. Khoo, K.Y. Lam, Nonlinear interaction between gas bubble and free surface, *Theoretical and Computational Fluid Dynamics* 25 (7) (1996) 607–628.
[9] R.H. Cole, *Underwater Explosion*, Princeton University Press, Princeton, NJ, 1948.
[10] C. Wang, B.C. Khoo, An indirect boundary element method for three-dimensional explosion bubbles, *Journal of Computational Physics* 194 (2–4) (2004) 451–480.
[11] Y.S. Dai, *Potential Flow Theory of Ship Motions in Waves in Frequency and Time Domain*, National Defense Industries Press, Beijing, 1998.
[12] T.S. Lundgren, N.N. Mansour, Vortex ring bubbles, *Journal of Fluid Mechanics* 224 (2–3) (1991) 177–196.
[13] J.P. Best, The rebound of toroidal bubbles, *IUTAM Symposium on Bubble Dynamics and Interface Phenomena*, 1994.
[14] S.G. Zhang, J.H. Duncan, G.L. Chahine, The final stage of the collapse of a cavitation bubble near a rigid wall, *Journal of Fluid Mechanics* 257 (4) (1993) 147–181.
[15] S. Zhang, J.H. Duncan, On the nonspherical collapse and rebound of a cavitation bubble, *Physics of Fluids* 6 (7) (1994) 2352–2362.

[16] C.A. Brebbia, *The Boundary Element Method for Engineers*, Halstead Press, New York, 1978.
[17] S.A. Wilkerson, A Boundary Integral Approach to Three-dimensional Underwater Explosion Bubble Dynamics, PhD Thesis, Department of Mechanical Engineering, The Johns Hopkins University, 1990.
[18] E. Klaseboer, K.C. Hung, C. Wang, C.W. Wang, B.C. Khoo, P. Boyce, S. Debono, H. Charlier, Experimental and numerical investigation of the dynamics of an underwater explosion bubble near a resilient/rigid structure, *Journal of Fluid Mechanics* 537 (1) (2005) 387–413.
[19] Y.J. Liu, On the simple-solution method and non-singular nature of the BIE/BEM review and some new results, *Engineering Analysis with Boundary Elements* 24 (5) (2000) 789–795.
[20] C. Wang, B.C. Khoo, K.S. Yeo, Elastic mesh technique for 3D BIM simulation with an application to underwater explosion bubbles, *Computers and Fluids* 32 (9) (2003) 1195–1212.
[21] J. Bjerknes, *Fields of Force*, Columbia University Press, New York, 1966.